Rev. Int. Contam. Ambie. 38 (Sustainable Architecture and Urban Environment) 143-161, 2022
https://doi.org/10.20937/RICA.54430

HEAT TRANSFER ANALYSIS OF CELLULAR HEAT EXCHANGER BASED ON A FRESH FRACTAL VICSEK MODEL BY GALERKIN FINITE ELEMENT METHOD

Análisis de transferencia de calor de un intercambiador celular de calor con base en un modelo fresco del fractal de Vicsek por medio del método de elementos finitos de Galerkin

Ma ZHUQIAO[1]*, Zhang YUFAN[1], Huang YIJIE[1]and Ren ZHEYU[1]

[1] School of Intelligent Manufacturing, Nanjing University of Science and Technology Zijin College, Nanjing 210046, China

*Corresponding author email: mazenxieco2371@163.com

(Received: June 2021; accepted: January 2022)

Key words: heat transfer, cellular heat exchanger, Vicsek fractal, Galerkin finite element methods, tessellation method

ABSTRACT

The energy density is increasing in modern industry, and the lack of heat transfer efficiency is one of the fatal problems of current equipment, which seriously affects the improvement of production level. The cellular heat exchanger is a kind of heat exchanger used in different fields. It plays an irreplaceable role in energy saving, efficiency improvement and reducing pressure drop. However, when the geometric shape of the fractal heat exchanger is very complex, the heat transfer analysis is impossible or difficult to show. Therefore, the objective of this project is to solve the difficulty of analysis on complex fractal heat exchangers and have a better representation of the physics. A totally fresh tessellation method, which can be used to analyze complex fractal heat exchangers, is introduced in this essay. By the research process, surjective hole-fill maps for Vicsek fractal were established, and Vicsek fractal was represented by continuous tessellations, and the fractal Vicsek model was expressed by continuous subdivision. The transfer theory on fractals and Galerkin finite element method were used to analyze the heat transfer of fractals and tessellations. The results of two analyses, the fractal model and the tesselation model, were almost the same, and confirm the function of the tessellation method in the analysis of complex heat exchangers. Furthermore, it provides a new way to solve the difficult problem of heat transfer analysis of complex geometric heat exchangers.

Palabras clave: transferencia de calor, intercambiador de calor celular, Fractal de Vicsek, métodos de elementos finitos de Galerkin, método de teselación

RESUMEN

La densidad de energía está aumentando en la industria moderna, y la falta de eficiencia de transferencia de calor es uno de los problemas fatales de los equipos actuales, que afecta seriamente la mejora del nivel de producción. El intercambiador de calor celular es un tipo de intercambiador de calor utilizado en diferentes campos. Desempeña un papel insustituible en el ahorro de energía, la mejora de la eficiencia y la reducción de la caída de presión. Sin embargo, cuando la forma geométrica del intercambiador de

calor fractal es muy compleja, el análisis de transferencia de calor es imposible o difícil de mostrar. Por lo tanto, el objetivo de este proyecto es resolver la dificultad de análisis en intercambiadores de calor fractales complejos y tener una mejor representación de la física. En este ensayo se presenta un método de teselación totalmente fresco, que se puede utilizar para analizar intercambiadores de calor fractales complejos. Mediante el proceso de investigación, se establecieron mapas de relleno de agujeros para Vicsek fractal, y el fractal de Vicsek estuvo representado por teselaciones continuas, y el modelo de Vicsek fractal se expresó por subdivisión continua. La teoría de transferencia de fractales y el método de elementos finitos de Galerkin se utilizaron para analizar la transferencia de calor de fractales y teselaciones. Los resultados de los dos análisis, el modelo fractal y el modelo de teselación, fueron casi los mismos, y confirman la función del método de teselación en el análisis de intercambiadores de calor complejos. Además, proporciona una nueva forma de resolver el difícil problema del análisis de transferencia de calor de intercambiadores de calor geométricos complejos.

INTRODUCTION

Compared with other types of heat exchanger, the cellular heat exchanger is a new type of high-efficiency heat transfer equipment (Davey et al. 2013, Higashiyama et al. 2019, Ma et al. 2021). However, due to its complex geometry, it is difficult to analyze this kind of heat exchanger. This essay will examine the way in which thermal physics pertaining to fractal heat exchangers (Chowdhury et al. 2018, Li et al. 2021). The methodological approach taken in this study is a mixed methodology based on the application of transport theory to fractals. Vicsek fractal was used to represent the cellular structure and a mapping strategy invoking a hole-fill map concept to a tessellated continuum (Kounadis et al. 2021, Kercher et al. 2021). This paper began with the research status of the cellular heat exchanger and the development of research methods, and backgrounds for the tessellation method proposed were displayed, which gave the basic theory to deduce the method. The Model section began by laying out the theoretical dimensions of the research, and discussed how to construct hole-fill maps for fractals. Moreover, hole-fill maps for fractal Vicsek are constructed. The continuous tessellation, which can represent fractal Vicsek, can be formed by hole-fill maps. The third chapter is concerned with the methodology used for this study. Based on the transfer theory of fractal, the material properties of tessellation can be obtained, which can be used for finite element analysis of the tessellation continuum (Kounadis et al. 2021, Li et al. 2021). The fourth section presents the findings of the research. Because the fractal can be represented by the tessellation, therefore, the results on the fractal and the tessellation should be the same (Jing et al. 2018). In order to test whether this method is correct or suitable for complex fractals, heat transfer analysis on the fractal heat exchangers and corresponding tessellations were carried out using Abaqus software and the results for the fractal and corresponding tessellation were compared.

Existing works on cellular heat exchangers

A tessellated continuum approach

In 2015, Davey, Prosser and Jiang did a research on how to analyze the heat transfer through fractal-like porous media (Davey et al. 2015). In their report, the cellular structure was represented by a fractal or a pre-fractal and the heat transfer can be achieved by analyzing the tessellated continuum. In the essay, the transport theory for fractals is introduced, and this theory is coupled to hole-fill mapping strategy, then the analysis is done on a tessellated continuum. An iterated function is used to construct the hole-fill map, which is quite similar to that in the fractal generation process. After mapping, the analytical and numerical continuum solutions can be applied to the fractal media and results can be obtained from the analysis on the tessellated continuum.

From the paper written by Davey et al., a solution can be got that heat transfer analysis on a tessellated continuum is feasible for simple fractals (Davey et al. 2015) . There are lots of methods that can be learned from their project and used in my project after optimization.

Theoretical study on the thermal-hydraulic performance of cellular structure

In 2007, Tian, Lu, Hodson, Queheillalt and Wasley did research on the thermal-hydraulic performance of the cellular structure by using experimental and theoretical methods. The cellular structure in their research is cooled by both air and water in forced convection (Tian et al. 2007).

Under the condition of high Reynolds number, the friction coefficient, which is based on unit pore size, is mainly determined by the opening ratio. The transfer of heat is determined by the conduction of the solid ligaments and by forced convection to the applied airflow or water flow; The heat transfer performance of the diamond directional structure is better than that of other structures; When Reynolds number is constant, heat transfer is mainly determined by porosity and surface area density; When the porosity is given, the heat dissipation rate increases with the increasing of the surface area density. However, when the surface area density is constant, there is an optimal porosity, which can obtain the maximum heat dissipation.

Numerical simulation

In 2010, Dorea and co-workers performed a numerical simulation of a porous material plate under a laminar impingement jet. Their work greatly improves accuracy (Dórea et al. 2010). The major limitation of this study is that the assumption of cellular structure distortion and dispersion mechanism was ignored. This is only helpful to analyze the geometric effect of cellular structure.

Dawood et al. (Teamah et al. 2011) conducted a numerical simulation of horizontal tubes filled with porous materials partially or completely under laminar forced convection. Three different cases were analyzed. The first case is that the porous material is placed on the central line of the pipeline, and the porous material is cylindrical. The second case is that porous materials are annular. In the third case, the porous material is placed at $z = 0.05L$ from the pipe inlet with a cylindrical shape. It is found that the thermal performance of the porous material decreases with the increase of the radius of the porous material. The first porous material has the best heat transfer performance and the highest pressure drop.

Galerkin finite element method in tessellated continuum mechanics

In 2016, Davey tested the hypothesis that the tessellation used in tessellated continuum mechanics can form a mesh in a continuous Galerkin finite element method (Davey et al. 2016). A distinctive feature of the tessellation is that it can possess highly distorted elements yet, as a consequence of associated anisotropy in material properties—can still return accurate results. This study shows that thermal analysis on pre-fractals can be achieved indirectly through analysis on a tessellated continuum using a Galerkin finite element method; the accuracy of the Galerkin finite element method is reasonable (less than a few percent for the examples considered) although it requires reasonably high heat transfer coefficients to be applied to cooling channels to reduce modeling error.

The techniques and methods related to my essay

Transport theory of fractals

In 2005, Tarasov considered using fractional integral to describe fractal media. The equation of continuity for fractal media is shown below

$$\frac{\partial \rho(R_t,t)}{\partial_t} + V_t \frac{\partial \rho(R_t,t)}{\partial R_t} + \frac{(D-3)(R_t,V_t)}{|R_t|^2} \rho(R_t,t) + \rho(R_t,t) \frac{\partial V}{\partial R_t} = 0. \quad (1)$$

Where D is mass dimension; V_t is the volume of the region.

And when the medium is homogeneous, the equation can be simplified as

$$\frac{(D-3)(R_t,V_t)}{|R_t|^2} \rho(R_t,t) + \rho(R_t,t) \frac{\partial V_t}{\partial R_t} = 0. \quad (2)$$

The R_t in the equation can be calculated as

$$\int_{W_t} \rho(R_t,t) d\mu D(R_t) = \int_{W_0} \rho(R_0,0) d\mu D(R_0). \quad (3)$$

Where R_0 in this equation is a Lagrange variable.

In the same year, Tarasov described the dynamic processes in the fractal medium by using the fractional integrals that were produced by him. The fractional generalization of the equilibrium equations of momentum density, internal energy and mass density were derived. The real fractal structure can be disregarded in many problems, and the continuous fractional model can be used to replace the real problem.

In 2007, Ostoja-Starzewski developed the continuum equation of the second law of fractal thermodynamics, which was also deduced by Ziegler's thermodynamic theory. When the thermodynamic condition is orthogonal, the essential law of elastic dissipative fractal medium can be deduced by generalized fractional integrals.

Hole-filling method

In 2013, Davey and Prosser described an analytical method for dealing with heat transfer problems in pre-fractional and fractal domains(Dórea et al. 2010). This method is based on the existing mappings between pre-fractals and continuum, so the mappings

between pre-fractals and continuum are the focus of its research. The solution method is simple. As long as the space parameters of the continuous solution are changed, the pre-fractal and fractal solutions can be obtained when the map already exists.

Background for the study

This section mainly describes the background of research methods, which provides the basis for the research work of this paper. The conductive heat transfer on a continuum body can be well described by Fourier's law of heat conductivity. Firstly, mapping between pre-fractals and the continuum should be established. The transfer equation can be linked to the continuum. When the material properties on the fractal are known, the material properties on the continuum can be obtained. After that, the analytical theory on the continuum can be used on the established continuum and the results collected from the continuum can be used to represent the results on the fractals.

One-dimensional fractal rod

For a rod with an initial length of l_0, the required Cantor set is generated by the self-similar contraction mappings

$$S_1(x)=\frac{x}{3}, S_2(x)=\frac{2l_0+x}{3}. \tag{4}$$

where E_2 = [0, l_0] and the linking between E_0 and E_1 is given by

$$E_1 = S_1(E_0)\cup S_2(E_0) = \left[0,\frac{l_0}{3}\right]\cup\left[\frac{2l_0}{3},l_0\right]. \tag{5}$$

And E_2 can be got similarly by

$$E_2 = S_1(E_1)\cup S_2(E_1) = \left[0,\frac{l_0}{9}\right]\cup\left[\frac{2l_0}{9},\frac{l_0}{3}\right] \cup\left[\frac{2l_0}{3},\frac{7l_0}{9}\right]\cup\left[\frac{8l_0}{9},l_0\right]. \tag{6}$$

Cantor dust is shown in **figure 1**

From **figure 1**

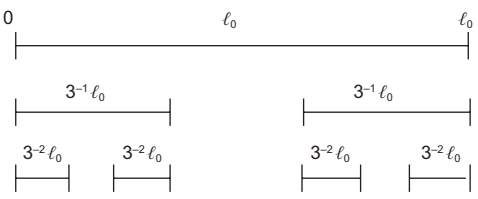

Fig. 1. Pre-fractals for the Cantor dust.

$$x_k(s) = \left(\frac{3}{2}\right)^k \int_0^s u_k(r)dr. \tag{7}$$

$$u_k(s)=\begin{cases} 1 & if\ s\in E_k \\ 0 & if\ s\in[0,l_0]/E_k \end{cases}. \tag{8}$$

This equation relates the fractal to the continuum. The differential equation, which relates the differential of E_k to the length differential of E_0 is shown below

$$dx_k(s) = \left(\frac{3}{2}\right)^k u_k(s)ds. \tag{9}$$

For the Cantor dust above, the scaling factors $|S_1|$ = $|S_2|$ = 1/3, so the fractal dimension can be given by

$$\left(\frac{1}{3}\right)^{D_1} + \left(\frac{1}{3}\right)^{D_1} = 1. \tag{10}$$

For the above bars, mass is assumed uniformly distribute over the bar, and the mass for the initial bar is assumed as M_0. The mass for the element in the E_k can be given as $M_k = 2^{-k} M_0$. And this can be written as

$$\frac{\left(\frac{M_k}{M_0}\right)}{\left(\frac{l_k}{l_0}\right)} = \left(\frac{V_k}{V_0}\right)^{D_1-1}. \tag{11}$$

l_k in the equation is the length of the element in the E_k, l_0 is the initial length of the bar, V is the volume of the bar. The solution can be obtained by substituting the above equation into Equation 9

$$dx_k = \left(\frac{l_k}{l_0}\right)^{D_1-1} u_k(s)ds. \tag{12}$$

One-dimensional steady-state fractal solutions

Heat transfer will be carried out on the established continuum model, and the problem has been transformed into a steady-state problem without the heat source, and the obtained result can represent the results for fractals. The temperature at x = 0 is assumed as T_0 and at x = l_0 is assumed as T_l. Satisfy the differential equation $K_0T'' = 0$. the temperature for the kth pre-fractal can be represented as

$$T_k(s) = T\bullet x_k(s). \tag{13}$$

Thus available

$$T_k(s) = T_0 + \frac{\Delta T_0}{l_0}\left(\frac{l_k}{l_0}\right)^{D_1-1}\int_0^s u_k(r)dr. \tag{14}$$

The differential of Equation 13 and 14, the following equation can be got

$$\frac{dT_k}{ds}=\frac{dx_k}{ds}\frac{dT}{dx}=(\frac{3}{2})^k u_k\frac{dT}{dx}=(\frac{l_k}{l_0})^{D_1-1}u_k\frac{dT}{dx}. \quad (15)$$

$$\frac{d^2Tk}{ds^2}=\frac{d^2x_k}{ds^2}\frac{dT}{dx}+(\frac{dx_k}{ds})^2\frac{d^2T}{dx^2}=\left[(\frac{l_k}{l_0})^{D_1-1}u_k\right]^2\frac{d^2T}{dx^2}. \quad (16)$$

For the place where the solution is not satisfied, the heat flux should be matched by the appropriate specification of K_k

$$\frac{K_k}{K_0}=\frac{l_k}{l_0}\frac{\Delta T_0}{\Delta T_k}=(\frac{2}{3})^k=(\frac{l_k}{l_0})^{1-D_1}. \quad (17)$$

Where $l_k = l_0/3^k$ and $\Delta T_k = \Delta T_k/2^k$.

When the bar with a constant, uniform heat source Q per unit volume, the governing differential equation can be represented as $K_0T' + Q = 0$, and the solution can be written as

$$T(x)=T_0+\frac{\Delta T_0}{l_0}x-\frac{1}{2}\frac{Q}{K_0}x(x-l_0). \quad (18)$$

One-dimensional transient thermal problems

The transient behavior of the continuum rod, such as density and internal energy, can be described by the partial differential equation.

$$\rho_0 c_0\frac{\partial T_k}{\partial t}=K_0\frac{\partial^2 T}{\partial s^2}. \qquad \rho_k c_k\frac{\partial T_k}{\partial t}=K_k\frac{\partial^2 T_k}{\partial s^2}. \quad (19)$$

For the null region in the bar, there is no mass distributed, so the density follows

$$\rho_k=(\frac{l_k}{l_0})^{D_1-1}u_k\rho_0.$$

The internal energy is like the mass distribution on the fractal, and there is no energy exist in the null regions. Therefore, for an element in the E_k, the internal energy differential can be expressed as

$$\rho_0 c_0\Delta T(Adx_k)=\rho_k c_0\Delta T(Ads)=\rho_k c_k\Delta T_k(Ads). \quad (20)$$

The following solution can be got $c_0 = c_k$.

The temperature $T_k(s,t) = T(x_k(s),t)$ is a solution, and the differential equations are shown as Equation 15 and 16, substituting these equations into Equation 18. The following equation can be got

$$\rho_k c_k\frac{\partial T_k}{\partial t}=\rho_0 c_0(\frac{l_k}{l_0})^{D_1-1}u_k\frac{\partial T}{\partial t}= K_k\frac{\partial^2 T_k}{\partial s^2}=K_0(\frac{l_k}{l_0})^{D_1-1}u_k\frac{\partial^2 T}{\partial x^2}. \quad (21)$$

MODEL

Hole-fill maps

The key step to analyze fractal thermal performance is to construct hole-fill maps. The method introduced in the previous section for constructing the hole-filled map on one-dimensional bars is not easily applied to non-integrative sets, such as fractal Vicsek. Therefore, a method to construct the hole-fill maps through function composition is proposed in this chapter.

Construction of maps by function composition

The function composition method makes use of the inverse maps. For the E_1, the hole-fill map can be expressed as $P_1 \bullet S_1^{-1}(s)=\frac{3s}{2}, s\in[0,\frac{l_0}{2}]$ and $P_1 \bullet S_1^{-1}(s)=\frac{3s}{2}-\frac{l_0}{2}, s\in[\frac{2l_0}{3}, l_0]$.

Like the constructing for E_1, the hole-fill map for the E_2 is obtained by pre and post mapping operations on $P_1 \bullet S_1^{-1}$ and $P_2 \bullet S_2^{-1}$. E_2 can be got as

$$\begin{cases}P_1\bullet(P_1\bullet S_1^{-1})\bullet S_1^{-1}\\ P_1\bullet(P_2\bullet S_2^{-1})\bullet S_1^{-1}\\ P_2\bullet(P_1\bullet S_1^{-1})\bullet S_2^{-1}\\ P_2\bullet(P_2\bullet S_2^{-1})\bullet S_2^{-1}\end{cases}=\begin{cases}(\frac{3}{2})^2 s & \text{if s}\in\left[0,\frac{l_0}{9}\right]\\ -\frac{l_0}{4}+(\frac{3}{2})^2 s & \text{if s}\in\left[\frac{2l_0}{9},\frac{3l_0}{9}\right]\\ -l_0+(\frac{3}{2})^2 s & \text{if s}\in\left[\frac{6l_0}{9},\frac{7l_0}{9}\right]\\ -\frac{5l_0}{4}+(\frac{3}{2})^2 s & \text{if s}\in\left[\frac{8l_0}{9},\frac{9l_0}{9}\right]\end{cases} \quad (22)$$

The eight components of E_3 are easily obtained using the same construction.

Although this method seems a little difficult, the maps are generated directly as part of the Fractal and Tessellation formation process.

Construction maps for fractal Vicsek

The basic square is decomposed into nine squares in the three-by-three grids. The four squares at the corners are removed, and the other squares are left. Then the process is repeated.

The initial pre-fractal (E_0^s) for the fractal is a square, as shown in **figure 2**. The length of the initial pre-fractal is assumed as 1. The initial square is formed by 8 points, the points are denoted E_0^s, where

$$E_0^s=\left\{(0,0),\left(\frac{1}{2},0\right),(1,0),\left(1,\frac{1}{2}\right),(1,1),\left(\frac{1}{2},1\right),(0,1),\left(0,\frac{1}{2}\right)\right\}.$$

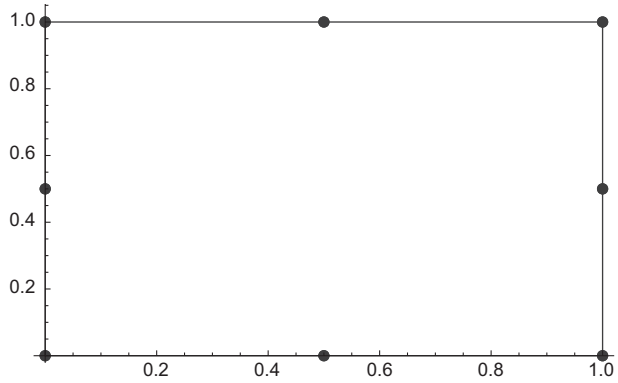

Fig. 2. The initial pre-fractal for Vicsek fractal.

In order to generate the hole-fill maps for the fractal Vicsek and calculate the thermal conductivity for the corresponding tessellation, the initial pre-fractal is meshed into eight triangles; therefore, an extra point is added in the middle of the square and three points can denote each triangle. The initial pre-fractal after being meshed is shown in **figure 3**.

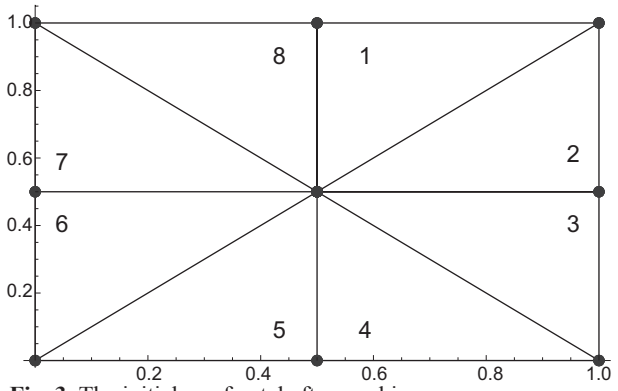

Fig. 3. The initial pre-fractal after meshing.

In order to form E_1^s, five maps are employed.

$$S_1(x,y)=\left(\frac{x}{3},\frac{y}{3}\quad\frac{1}{3}\right)$$

$$S_2(x,y)=\left(\frac{x}{3}+\frac{1}{3},\frac{y}{3}+\frac{1}{3}\right)$$

$$S_3(x,y)=\left(\frac{x}{3}+\frac{1}{3},\frac{y}{3}\right)$$

$$S_4(x,y)=\left(\frac{x}{3}+\frac{2}{3},\frac{y}{3}+\frac{1}{3}\right)$$

and $S_5(x,y)=\left(\frac{x}{3}+\frac{1}{3},\frac{y}{3}+\frac{2}{3}\right)$.

The first pre-fractal E_1^s can be formed by

$$E_1^s = S_1E_0^s \cup S_2E_0^s \cup S_3E_0^s \cup S_4E_0^s \cup S_5E_0^s.$$

In this article, the abbreviation E_1^s, E_2^s, E_3^s, E_4^s will be used to refer to first pre-fractal, second pre-fractal, third pre-fractal.

According to **figure 4**, it is clear that S_1 transformed the initial pre-fractal E_0^s into the left square in **figure 4**.

Similarly, E_2^s, E_3^s can be formed in the same way used for forming the first pre-fractal. The second pre-fractal E_2^s and the third pre-fractal E_3^s are shown as **figure 5** and **figure 6**.

According to **figure 4**, there are four holes in the E_1^s; the basic principle to fill these holes is to fill the holes equally by the adjacent squares. As shown in **figure 7**, the triangle six and seven are filled by square one, the triangle eight and nine are filled by square three, the triangle 10 and 11 are filled by square four, and the triangle 12 and 13 are filled by square five.

The five corresponding cover maps for fractal Vicsek in the "Appendix".

The 40 maps displayed above transfer the first pre-fractal for fractal Vicsek shown in **figure 3** to the tessellation identified in **figure 8**. Replace the initial square in **figure 3** with the antiparallelogram in **figure 8** to reduce the squares of the initial shape. The corresponding maps transferred the square in **figure 3** to the tessellation shown in **figure 8**.

Similarly, the corresponding tessellation of the second and third pre-fractal are shown as **figure 9** and **figure 10**.

Transport equations for a fractal

When analyzing the physical processes on the fractals, the direct derivation of the governing partial differential equation cannot solve the problem simply. In this case, an effective choice is to start the analysis from the integral form of the transfer equation and then proceed to the strong form.

Integral forms of transport equation

The integral forms of the continuum transfer equations are applied to the fractal and corresponding tessellation.

$$\frac{d}{dt}\int_{\Omega_s}\rho_s\Psi_s dV_s+\int_{\Gamma_S}\rho_s\Psi_s v_s\cdot n_s d\Gamma_s = -\int_{\Gamma_S}J_s\cdot n_s d+_s\Gamma\int_{\Omega_S}\rho_s b_s dV_s. \tag{23}$$

$$\frac{d}{dt}\int_{\Omega_r}\rho_r\Psi_r dV_r+\int_{\Gamma_r}\rho_r\Psi_r v_r\cdot n_r d\Gamma_r = -\int_{\Gamma_r}J_r\cdot n_r d\Gamma_r+\int_{\Omega_r}\rho_r b_r dV_r. \tag{24}$$

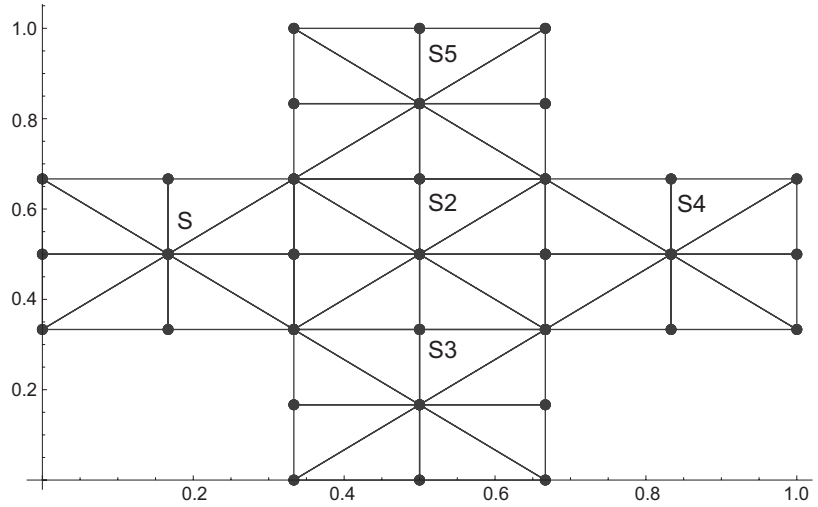

Fig. 4. The first pre-fractal for fractal Vicsek.

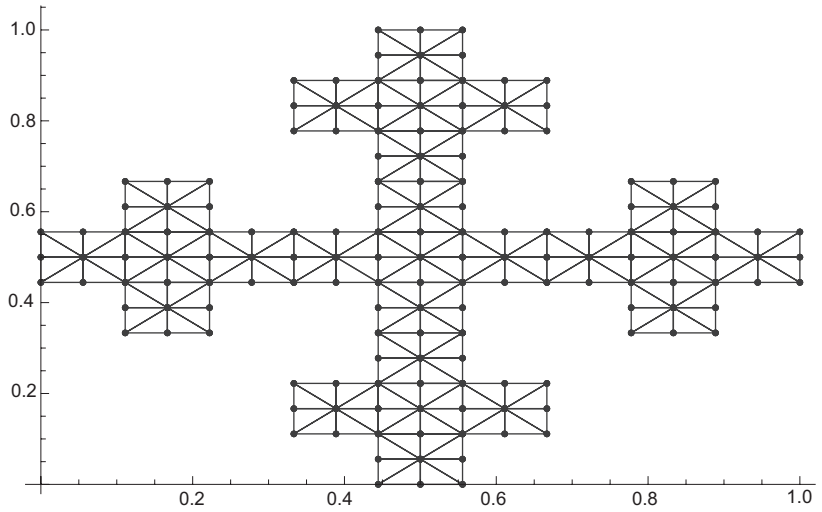

Fig. 5. The second pre-fractal for fractal Vicsek.

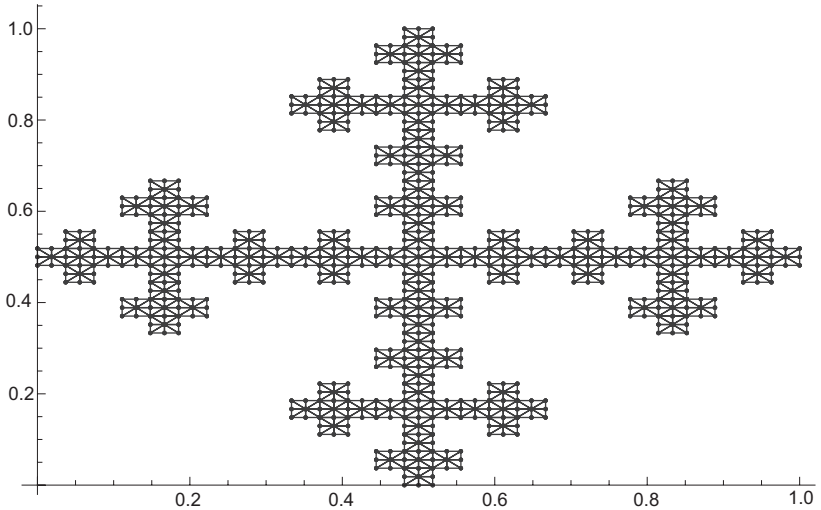

Fig. 6. The third pre-fractal for fractal Vicsek.

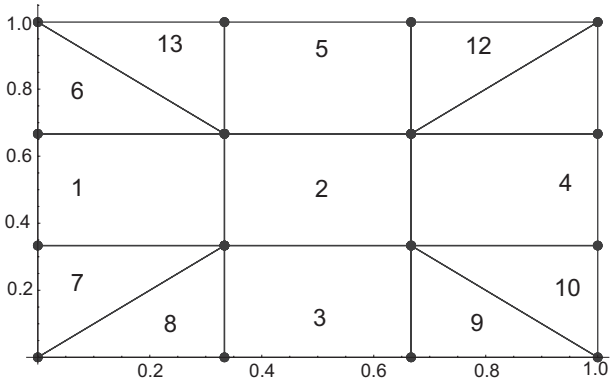

Fig. 7. Hole filling principle for the first pre-fractal.

Where ρ is the density, v is the velocity of the material, $J \cdot n$ is a flux, b is a source term.

Equation 23 can relate to Equation 24 by the hole-fill maps between the fractal and the corresponding tessellation. Analyzing the geometry of the structures can get Nason's differential relationships:

$$dV_r = |F|\,\mu_k dV_s,\ d\Gamma_r = |F|\,\mu_k{}^{\Gamma} d\Gamma_s \cdot F^{-1},$$
$$F_{ij} = \partial x_i / \partial s_j,\ d\Gamma_s = n_s d\Gamma_s,\ d\Gamma_r = n_r d\Gamma_r.$$

Substitution of these Nason's differential relationships into the Equation 24, the following equation can be got

$$\frac{d}{dt}\int_{\Omega_S} \rho_r \Psi_r |F|\,\mu_k dV_s + \int_{\Gamma_S} \rho_r |F| \Psi_r \mu_k F^{-1} \cdot v_r \cdot d\Gamma_s = \int_{\Gamma_S} |F_X{}^*|\,\mu_k F^{-1} \cdot J_r \cdot d\Gamma_s + \int_{\Omega_S{}^*} \rho_r |F|\,\mu_k b_r dV_s. \quad (25)$$

The mass-conserving map makes the mass in the fractal the same as the mass of the tessellation. So, the following equation should be satisfied.

$$\rho_r dV_r = \rho_s dV_s. \quad (26)$$

Substitute the Nason's differential relationship into Equation 26, then the relationship between ρ_r and ρ_s can be expressed as $\rho_r |F| \mu_k = \rho_s$.

By comparing Equation 25 and 23, it is easy to

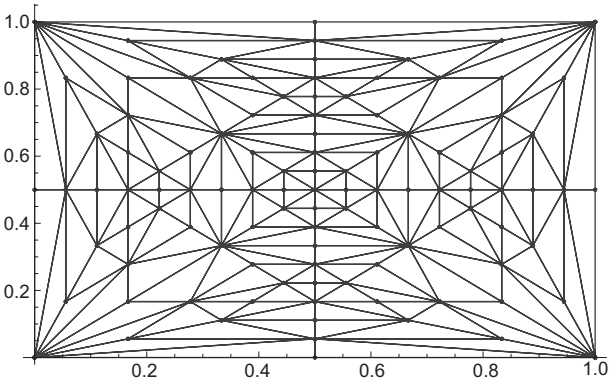

Fig. 9. The corresponding tessellation for the second pre-fractal of fractal Vicsek.

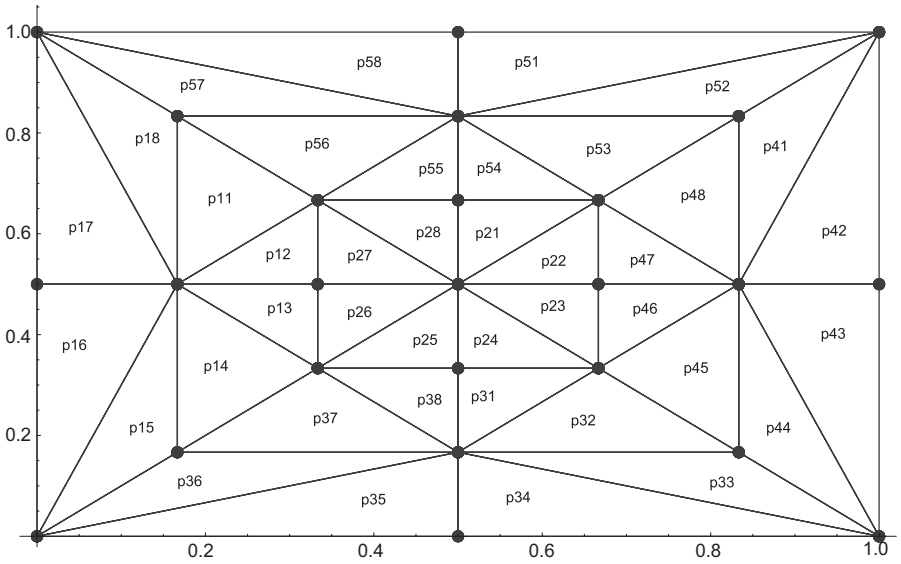

Fig. 8. The corresponding tessellation for the first pre-fractal of fractal Vicsek.

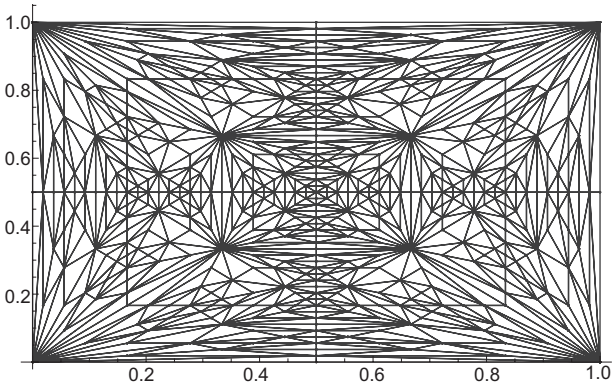

Fig. 10. The corresponding tessellation for the third pre-fractal of fractal Vicsek.

achieve that $\Psi_r = \Psi_s$, $\rho_r |F|\mu_k = \rho_s$ and $|F|\ \mathrm{F}^{-1} \cdot J_r = J_s$, $b_r = b_s$.

Differential forms of transport equation

The associated partial differential equation for the transport Equation 24 is

$$\rho_r \frac{\partial \Psi_r}{\partial t} + \rho_r v_r \cdot \nabla \Psi_r = -div_r(J_r) + \rho_r b_{r'}. \quad (27)$$

In order to analyze the continuum tessellation, considering the heat transfer problem for the fractal, v_s and v_r are set equal to zero. Then the partial differential equation can be written as

$$\rho_r \frac{\partial h_r}{\partial t} = -div_r(K_r \cdot \nabla_r \theta_r) + \rho_r Q_r. \quad (28)$$

Where h_r is the specific enthalpy, K_r is the thermal conductivity of the fractal and Q_r is a heat source.

From the relationship got in the integral form of the transport equation, it follows that $b_r = b_s$, $\Psi_r = \Psi_s$, $\rho_r |F|\mu_k = \rho_s$, and $|F|\ F^{-1} \cdot J_r = J_s$. Then the relationship for the thermal equation can be easily got by analogy analysis, $Q_r = Q_s$, $h_r = h_s$, $\rho_r = |\mathrm{F}|^{-1} \rho_s \mu_k^{-1}$, and $q_r = |F|^{-1} F \cdot q_s$, where the heat flux can be expressed as $q_s = -K_s \cdot \nabla_s \theta_s$.

The relationship between the thermal conductivity of the fractal and that of the tessellation can be got: $K_r = |F|^{-1} F K_s F^T$.

THEORY: GALERKIN FINITE ELEMENT METHODS

The study of complex fractal heat exchangers is a difficult project. In this paper, a finite element method to transform the complex problem of solving differential equations into the problem of solving linear equations is applied. In this chapter, the application of Galerkin finite element method in this project will be introduced. (Hoq et al. 2020, Ye et al. 2020, Zhang et al. 2020)

Heat conduction and boundary conditions

The internal temperature of an object depends on internal heat exchange, heat exchange between the object and the external medium and time. Heat exchange inside an object can be expressed by Fourier Equation for thermal conduction. The Fourier Equation is

$$\rho c \frac{\partial T}{\partial t} = \frac{\partial}{\partial x}(K_x \frac{\partial T}{\partial x}) + \frac{\partial}{\partial y}(K_y \frac{\partial T}{\partial y}) + \frac{\partial}{\partial z}(K_z \frac{\partial T}{\partial z}) + Q. \quad (29)$$

Where ρ is density, c is specific heat capacity, K is thermal conductivity, T is the temperature, t is the time period and Q is the internal heat flux.

In order to calculate the temperature distribution inside the object, initial conditions and boundary conditions are also needed. The initial condition is the initial temperature distribution on an object. There are three types of boundary conditions.

The first type is the fixed temperature on the boundaries of the objects, which can be expressed as

$$T_b = T. \quad (30)$$

The second type is that the surface heat flux is known and can be expressed as

$$K_x \frac{\partial T}{\partial x} n_x + K_y \frac{\partial T}{\partial y} n_y + K_z \frac{\partial T}{\partial z} n_z = q_b. \quad (31)$$

The third type is the heat convection on the boundary of the object is ensured, which can be expressed as

$$K_x \frac{\partial T}{\partial x} n_x + K_y \frac{\partial T}{\partial y} n_y + K_z \frac{\partial T}{\partial z} n_z = h(T_f - T_b). \quad (32)$$

Where h is the heat transfer coefficient, T_f is the temperature of the media around the object and T_b is the boundary temperature of the object.

If the boundary condition and internal heat source are fixed, the temperature distribution of the object will not change after a period of time, which is called steady heat conduction. The steady-state heat conduction of a three-dimensional object can be expressed as

$$\frac{\partial}{\partial x}(K_x \frac{\partial T}{\partial x}) + \frac{\partial}{\partial y}(Ky \frac{\partial T}{\partial y}) + \frac{\partial}{\partial z}(K_z \frac{\partial T}{\partial z}) + Q = 0. \quad (33)$$

The steady-state heat conduction problem requires only boundary conditions and thermal conductivity of materials. After determining the

thermal conductivity and boundary conditions of the material, the temperature distribution of the object in the steady state can be calculated by the finite element method.

Finite element method for steady-state heat conduction problem

The finite element equations are established by Galerkin method because the coefficient matrix is symmetrical when Galerkin method is used.

The shape function is assumed as

$$\left[N\right]=\left[N_1N_2N_3\cdots N_n\right]. \tag{34}$$

The temperature for the nodes of the elements is assumed as

$$\left\{T\right\}^e=\left[T_1T_2\cdots T_n\right]. \tag{35}$$

Therefore, the internal temperature of elements can be expressed as

$$T=\left[N\right]\left\{T\right\}^e. \tag{36}$$

For the two-dimensional steady-state heat conduction problem, the steady-state equation can be written as

$$\frac{\partial}{\partial x}(K_x\frac{\partial T}{\partial x})+\frac{\partial}{\partial y}(K_y\frac{\partial T}{\partial y})+Q=0. \tag{37}$$

The first heat exchange boundary condition can be expressed as

$$T_b=T. \tag{38}$$

The second heat exchange boundary condition can be expresses as

$$K_x\frac{\partial T}{\partial x}n_x+K_y\frac{\partial T}{\partial y}n_y=q_b. \tag{39}$$

The third heat exchange boundary condition can be written as

$$K_x\frac{\partial T}{\partial x}n_x+K_y\frac{\partial T}{\partial y}n_y=h(T_f-T_b). \tag{40}$$

The weighted integral for an element is

$$\int_\Omega^e w_1\left[\frac{\partial}{\partial x}(K_x\frac{\partial T}{\partial x})+\frac{\partial}{\partial y}(Ky\frac{\partial T}{\partial y})+Q\right]d\Omega=0. \tag{41}$$

The following equations can be got by integration by parts

$$\frac{\partial}{\partial x}(w_1K_x\frac{\partial T}{\partial x})=\frac{\partial w_1}{\partial x}(K_x\frac{\partial T}{\partial x})+w_1\frac{\partial}{\partial x}(K_x\frac{\partial T}{\partial x}).$$

$$\frac{\partial}{\partial y}(w_1K_y\frac{\partial T}{\partial y})=\frac{\partial w_1}{\partial y}(K_y\frac{\partial T}{\partial y})+w_1\frac{\partial}{\partial y}(K_y\frac{\partial T}{\partial y}).$$

By using Green Theorem, the weighted integral equation in an element can be written as

$$\begin{aligned}&-\int_\Omega^e\left[\frac{\partial w_1}{\partial x}(K_x\frac{\partial T}{\partial x})+\frac{\partial w_1}{\partial y}(K_y\frac{\partial T}{\partial y})-w_1Q\right]\\&d\Omega+\oint_\Gamma w_1\left(K_x\frac{\partial T}{\partial x}n_x+K_y\frac{\partial T}{\partial y}n_y\right)d\Gamma=0.\end{aligned} \tag{42}$$

By using Galerkin method, the weight function is chosen as $w_1 = N_i$.

The internal temperature distribution in the elements and heat exchange boundary conditions are substituted into Equation 42, and the following equation can be obtained.

$$\begin{aligned}&\int_\Omega^e\left[\frac{\partial N_i}{\partial x}(K_x\frac{\partial\left[N\right]}{\partial x})+\frac{\partial N_i}{\partial y}(K_y\frac{\partial\left[N\right]}{\partial y})\right]\\&\left\{T\right\}^e d\Omega-\int_\Omega^e N_iQd\Omega-\int_{\Gamma_2}^e N_iq_sd\Gamma+\\&\int_{\Gamma_3}^e N_ih\left[N\right]\left\{T\right\}^e d\Gamma-\int_{\Gamma_3}^e N_ihT_fd\Gamma=0.\end{aligned} \tag{43}$$

Through observation, the second heat transfer boundary condition and the third heat transfer boundary condition appear in Equation 43. The second heat exchange boundary condition is $-\int_\Gamma^e N_iq_sd\Gamma$ and the third heat exchange boundary condition is $\int_\Gamma^e N_ih[N]\{T\}^ed\Gamma-\int_\Gamma^e N_ihT_fd\Gamma$. However, the first boundary condition cannot be found in the above equation, because the weight function is selected as N_i, and the first boundary condition automatically satisfies.

Write Equation 43 into matrix form

$$\begin{aligned}&\int_\Omega^e\left[\left(\frac{\partial\left[N\right]}{\partial x}\right)^T(K_x\frac{\partial\left[N\right]}{\partial x})+\left(\frac{\partial\left[N\right]}{\partial y}\right)^T(K_y\frac{\partial\left[N\right]}{\partial y})\right]\\&\left\{T\right\}^e d\Omega-\int_\Omega^e\left[N\right]^TQd\Omega-\int_{\Gamma_2}^e\left[N\right]^Tq_sd\Gamma+\\&\int_{\Gamma_3}^e\left[N\right]^Th\left[N\right]\left\{T\right\}^e d\Gamma-\int_{\Gamma_3}^e\left[N\right]^ThT_fd\Gamma=0.\end{aligned} \tag{44}$$

Write Equation 57 into finite element form

$$\left[K\right]^e\left\{T\right\}^e=\left\{P\right\}^e. \tag{45}$$

Where $[K]^e$ is the temperature stiffness matrix for the element, $\{T\}^e$ is temperature at each element node and $\{P\}^e$ is thermal load vector.

For a specific element, temperature stiffness matrix $[K]^e$ and thermal load vector $\{P\}^e$ can be written as

$$K_{ij}=\int_{\Omega}^{e}\left(K_x\frac{\partial N_i}{\partial x}\frac{\partial N_j}{\partial x}+K_y\frac{\partial N_i}{\partial y}\frac{\partial N_j}{\partial y}\right)d\Omega+\int_{\Gamma_3}^{e}hN_iN_jd\Gamma. \quad (46)$$

$$P_i=\int_{\Gamma_2}^{e}N_iq_sd\Gamma+\int_{\Gamma_3}^{e}N_ihT_fd\Gamma+\int_{\Omega}^{e}N_iQd\Gamma. \quad (47)$$

If the element is not on the object boundary, Equation 46 and 47 can be simplified as

$$K_{ij}=\int_{\Omega}^{e}\left(K_x\frac{\partial N_i}{\partial x}\frac{\partial N_j}{\partial x}+K_y\frac{\partial N_i}{\partial y}\frac{\partial N_j}{\partial y}\right)d\Omega.$$

$$P_i=\int_{\Omega}^{e}N_iQd\Gamma$$

The weighted integral equation of the whole object is the sum of the integral equations of each element

$$\int_{\Omega}^{e}\left[\left(\frac{\partial[N]}{\partial x}\right)^T(K_x\frac{\partial[N]}{\partial x})+\left(\frac{\partial[N]}{\partial y}\right)^T(K_y\frac{\partial[N]}{\partial y})\right]\{T\}^e d\Omega-\sum_e\int_{\Omega}^{e}[N]^TQd\Omega-\sum_e\int_{\Gamma_2}^{e}[N]^Tq_sd\Gamma+\sum_e\int_{\Gamma_3}^{e}[N]^Th[N]\{T\}^e d\Gamma-\sum_e\int_{\Gamma_3}^{e}[N]^ThT_fd\Gamma=0. \quad (48)$$

The overall stiffness matrix equation is obtained by direct addition of a local number and overall number.

RESULTS

Heat transfer analysis on fractal Vicsek

The heat transfer analysis of the cellular heat exchanger with the same cross-section of fractal Vicsek was carried out. Three heat exchangers are analyzed here.(Xu 2019, Deng et al. 2020) The cross-section of the first heat exchanger is the first pre-fractal of the fractal Vicsek, and the cross-section of the second heat exchanger is the second pre-fractal of the fractal Vicsek. The cross-section of the third heat exchanger is the third pre-fractal of the fractal Vicsek.

The material properties, geometries and working load of the heat exchangers

The sections of the heat exchangers, which are analyzed here, are the pre-fractals of the fractal Vicsek. Assuming the heat exchanger is made of Aluminum, 6061, Temper-T4 and given the material properties are shown in **table I**. The cross-section geometry of the heat exchanger is 1m*1m, and the length of the heat exchanger is 1 m.

TABLE I. MATERIAL PROPERTIES FOR ALUMINUM, 6061, TEMPER-T41.

Conductivity (W/(m•K))	Density (kg/m^3)	Specific Heat (J/kg•K)
154	2710	1256

The boundary operating temperature of 303K was determined. Water was selected for heat exchangers as the coolant. It was assumed that the flow rate of water is 0.1 m/s, the water temperature is 293 K and the body heat of the heat exchanger is 10 W/m^2.

Heat transfer coefficient between water and the heat exchangers

The properties for water at 293 K are shown in the **table II**.

To calculate the heat transfer coefficient, the flow state of the water must be determined first. Therefore, the Reynolds numbers for the pre-fractals were calculated. The equation for calculating the Reynolds number is shown below

$$\mathrm{Re}=\frac{\rho\upsilon d}{u}. \quad (49)$$

Where ρ is the density of the water, υ is the velocity of the water, d is the equivalent diameter and u is the viscosity of the water.

When the cross-section shape is not a circle, for the purpose of calculation of the Reynolds number, the equivalent diameter was used. The equation for the equivalent diameter is $d = 4A/P$.

TABLE II. PROPERTIES FOR WATER AT 293 K.

Velocity (m/s)	Specific heat J / (kg•K)	Thermal conductivity W / (m•K)	Density kg/m^3	Viscosity (Pa.s)
0.1	4200	0.599	998.2	$1.003 * 10^3$

Where A is the square of the cross-section of the holes. P is the wetted perimeter, which is the contact perimeter of the cross section between fluid and holes.

When the cross-section of the heat exchanger is the first pre-fractal of fractal Vicsek, the square for the cross-section of the hole is 1/9 m^2, and the wetted perimeter is 4/3 m^2. So, the equivalent diameter for the hole is $d_1 = 4A/P = 1/3\ m$.

When the cross-section of the heat exchanger is the second pre-fractal of the fractal Vicsek, the equivalent diameter for the hole can be calculated in the same way, and the equivalent diameter $d_2 = 14/45\ m$.

When the cross-section of the heat exchanger is the third pre-fractal of the fractal Vicsek, the equivalent diameter is $d_3 = 151/594\ m$

After the equivalent diameters for the holes of heat exchangers are calculated, the Reynolds numbers for the water flow in the heat exchangers can be calculated. The Reynolds number for the water flow in the heat exchanger, which has a cross-section of the first pre-fractal of the fractal Vicsek, can be calculated by Equation 62 and the value of the Reynolds number is 33 173.81.

When the cross-section of the heat exchanger is 2nd pre-fractal of the fractal Vicsek, the Reynolds number for the water flow can be calculated in the same way used to calculate the Reynolds number for the water in the heat exchanger, which has a cross-section of second pre-fractal of the fractal Vicsek, and the value for the Reynolds number is 30 962.22.

In the same way, the Reynolds number for the water flow in the heat exchanger, which has a cross-section of the third pre-fractal of the fractal Vicsek, can be calculated, and the value of it is 25 299.22.

The calculation results show that the flow Reynolds number of the three heat exchangers is more than 10 000, so the flow in the heat exchanger is turbulent. For the turbulent flow, Dittus-Boelter Equation can be used to calculate the turbulent flow. The Dittus-Boelter Equation is

$$Nu = 0.023\,\mathrm{Re}^{0.8}\,\mathrm{Pr}^{n}. \tag{50}$$

Where Nu is Nusselt number of the fluid and Pr is Prandtl number of the fluid. When the fluid is used to heat the heat exchanger, n in Equation 50 is 0.4, and when the fluid is treated as coolant, n in Equation 50 is 0.3.

There are several requirements when Dittus-Boelter Equation is used to calculate the heat transfer coefficient. First of all, the temperature between the fluid and the holes should be medium. Generally, the temperature difference of the medium when air is selected as the fluid is less than 50 ºC, and the temperature of the medium of water is not more than 20-30 ºC. Second, the Reynolds number should be between 10 000 and 120 000. Third, the Prandtl number should be between 0.7 and 120. The ratio of the length to the equivalent diameter of the heat exchanger should be greater than or equal to 60.

Unfortunately, the requirements cannot be satisfied sometimes. When the requirements cannot be satisfied, some corrections are needed when the Dittus-Boelter Equation is used. For the case studied in this paper, the temperature between the water and the heat exchanger is 10 ºC, less than the required temperature difference, so there is no need to use the correction factor. Meanwhile, the Prandtl number of the fluid here can be calculated as

$$\mathrm{Pr} = \frac{uc_p}{K}. \tag{51}$$

Equation 51 can be used to calculate the Prandtl number of the water used here and the value of it is 7.04.

The ratio between the length of the heat exchanger and the equivalent diameter is much smaller than the required value; therefore, the correction factor for entrance influence should be added on Equation 50

$$c_l = 1 + (\frac{d}{l})^{0.7}. \tag{52}$$

The correction factors for entrance influence for three different heat exchangers can be calculated, the correction factor for the first heat exchanger is 1.46, the correction factor for the second heat exchanger is 1.44 and that for the third heat exchanger is 1.38. For the cases studied here the value of n for Equation 50 is 0.3, and the Nusselt number can be expressed as

$$Nu = \frac{hd}{K}. \tag{53}$$

Where h is the heat transfer coefficient between the fluid and the wall, d is the equivalent diameter of the hole and K is the thermal conductivity. Then the heat transfer coefficient between the fluid and the walls can be calculated. The heat transfer coefficient in the three heat exchangers can be found in **table III**.

Numerical simulation and discussion

Abaqus setups for steady state

The two-dimensional analysis is used for the heat exchangers, because the features in the length direction are the same. Therefore, there is no need

TABLE III. PROPERTIES OF THE FLUID IN THE HEAT EXCHANGERS 2.

	First heat exchanger	Second heat exchanger	Third heat exchanger
d(m)	1/3	14/45	151/594
l(m)	1	1	1
Re	33173.81	30962.22	25299.22
Pr	7.04	7.04	7.04
c_1	1.46	1.44	1.38
Nu	249.35	232.72	189.83
h (W / (m²•K)	448.08	448.08	447.30

to do the three-dimensional analysis on the heat exchangers.

For the first heat exchanger, the cross-section is shown in **figure 5**. Five squares are established in the part, and the thermal conductivity of aluminum, 6061, Temper-T4 is added to the parts. In the assemble part, these five parts are merged together. The boundary for the heat exchanger is fixed temperature 303 K and this is added to the four boundaries of the heat exchanger. The load for the heat exchanger is body heat flux and the value of it is 10 W/m^2. The interaction between fluid and walls is surface film condition and this is added to the contact boundaries of the walls, which are interacted with water. The heat transfer coefficient is 448.08 (W/(m^2•K)) and the water temperature in Abaqus is 293 K. Mesh type for the heat exchanger is linear and mesh shape is a triangle, which is the same as the numerical finite element method introduced in Theroy section.

For the second heat exchanger, 25 squares are established in the part, and the other setups in the Abaqus are the same as setups in the first heat exchanger.

For the third heat exchanger, 125 squares are established in the part and the heat transfer coefficient is 447.30 (W/(m^2•K)). The other setups are the same as setups for the first heat exchanger.

Abaqus setups for transient state

Abaqus Setups for the transient state are very similar to those for steady state. The main difference between steady state and transient state is that the transient state increases the material density and the specific heat of the material. For the step in the transient state, the transient time period is set as 30 000 s. The increment size of Abaqus is 30 s, the maximum increment number is 1000, and the end step size is set when the temperature change is less than 0.0001 K.

Mesh sensitivity analysis

When the mesh size decreases, the accuracy of simulation will be increased, but the time cost of simulation will be increased. Therefore, the optimal mesh size is where the change tends to be stable. The following **figures**, **11-13**, are the simulation of the temperature at the turning point of the three heat exchangers in different mesh sizes. From this data,

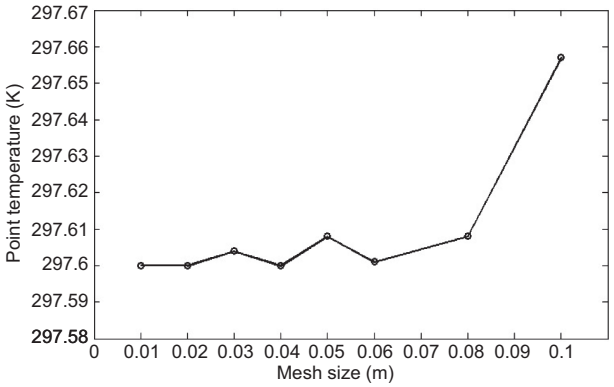

Fig. 11. The relationship between temperatures and mesh size for first heat exchanger.

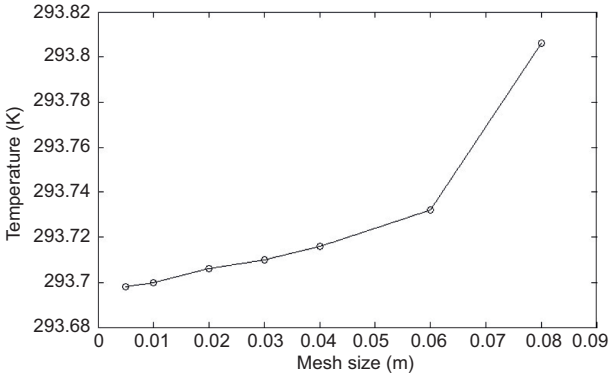

Fig. 12. The relationship between temperatures and mesh size for second heat exchanger.

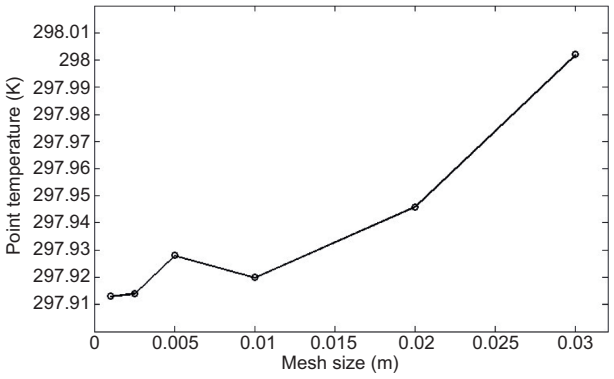

Fig. 13. The relationship between temperatures and mesh size for third heat exchanger.

we can see that the first heat exchanger is optimal when the mesh size is 0.02 m, the optimal size of the second type is 0.01 m and the optimal size of the third type is 0.0025 m.

RESULTS AND DISCUSSION

The steady state for the first heat exchanger is shown in **figure 14**.

The steady state for the second heat exchanger is shown in the **figure 15**.

The steady state for the third heat exchanger is shown in **figure 16** and **figure 17**. The temperature difference is not obvious and the temperature and geometry are symmetrical. This means that the temperature distribution at all four corners is the same. Thus, the left corner is shown in **figure 17** and can represent the other three corners.

It is apparent from the temperature distribution of the three heat exchangers above that the temperature difference on the heat exchanger increases as the complexity of the heat exchanger increases. The lowest temperature on the first heat exchanger is 297.5 K, and the lowest temperature on the second and third heat exchangers is about 293 K, which is almost the temperature of the coolant.

The temperature changes at the midpoint of each heat exchanger in the cooling process are shown in **figures 18**, **19** and **20**.

For the first heat exchanger, the temperature in the middle point decreased from 303 K to 298.272 K and it cost 4170 s to reach the steady state. For the second heat exchanger, 2490 s was used to reach the steady state and the temperature at the steady state is 293.77 K. For the third heat exchanger, the time period for reaching the steady state is 1110s and the temperature is 293.03 K. In summary, as the complexity increases, the time used to reach the steady state is sharply decreased.

Heat transfer analysis on the corresponding tessellation

The cross-section of the first heat exchanger, which has been analyzed above, can be transferred to the corresponding tessellation as shown in **figure 9**. Ideally, given the same conditions as for the first heat exchanger, the result in the corresponding area should be the same as for the first heat exchanger.

Abaqus setups

In the same way, two-dimensional analysis is used for the corresponding tessellation.

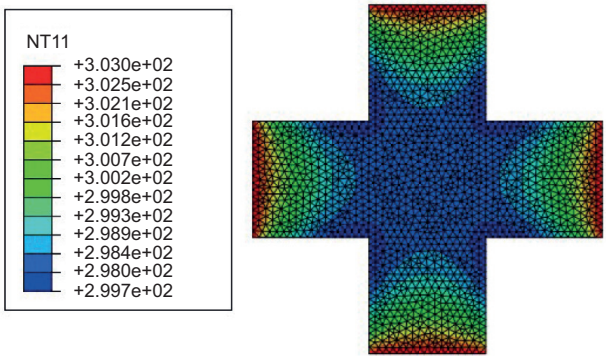

Fig. 14. The steady state for the first heat exchanger.

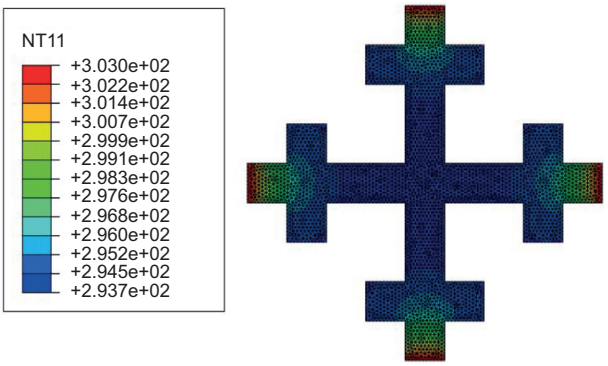

Fig. 15. The steady state for the second heat exchanger.

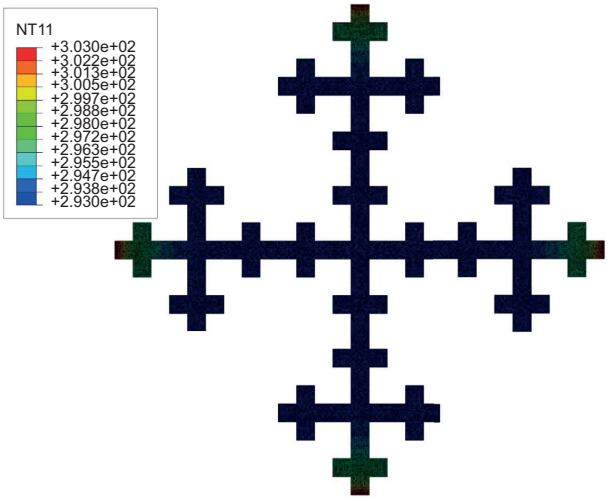

Fig. 16. Temperature distributions for the third heat exchanger.

The coordinates for 40 triangles can be obtained from the Mathematica program, and by using the coordinates; the 40 triangles can be constructed in the Abaqus. The original thermal properties for the

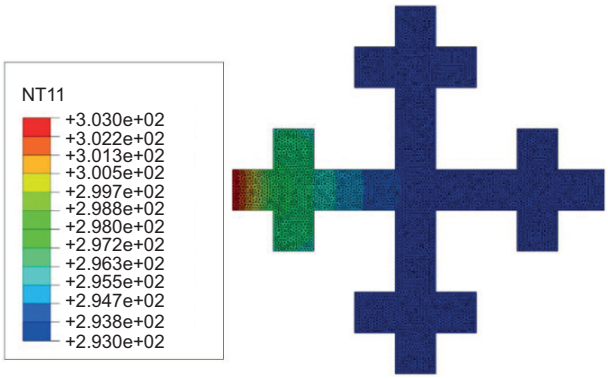

Fig. 17. Temperature distributions on the left corner.

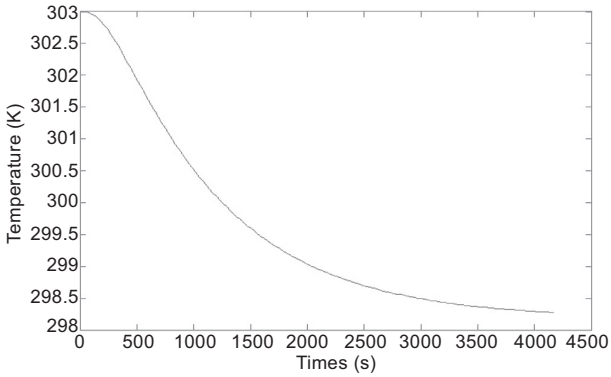

Fig. 18. The temperature change in the middle point of the first heat exchanger.

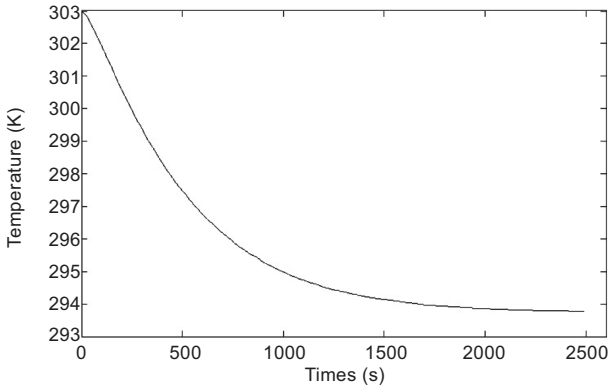

Fig. 19. The temperature change in the middle point of the second heat exchanger.

pre-fractals are assumed as 1 (W/(m•K)). Global material orientation is used when material properties are added to the parts. The first pre-fractal is constructed by five squares; therefore, these 40 triangles are merged into corresponding five parts, but the boundaries of each triangle are kept in assemble.

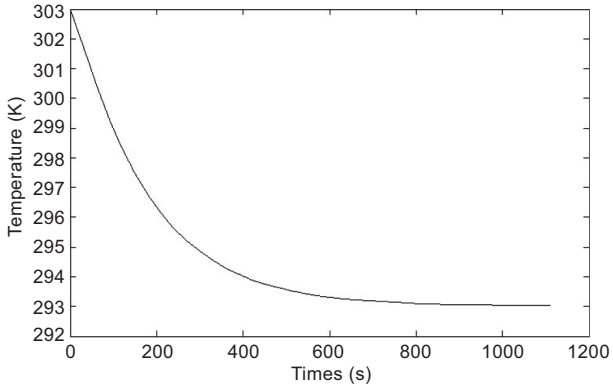

Fig. 20. The temperature change for the middle point of the third heat exchanger.

In order to make the load conditions on the tessellation the same as the corresponding pre-fractal, the body heat flow, boundary conditions, and heat exchange with water should be the same. The same fixed temperature 303 K is added as the boundary condition on the corresponding boundary of the tessellation. For the body heat, in order to keep the total amount the constant, it is easy to get that the equivalent body heat flux for the tessellation is 5.56 W/m^2. For the interaction between water and heat exchanger, in order to keep the total heat transfer amount the same, the following equation should be satisfied:

$$h_f \Delta TS_f = h_t \Delta TS_t. \quad (54)$$

Where h_f and h_t is the heat transfer coefficient for the pre-fractal and tessellation respectively and S is the contact area between fluid and heat exchanger. The heat transfer coefficient for the corresponding contact area in the tessellation should be 316.84 W/(m^2•K).

Mesh sensitive

In order to obtain the best mesh size of the heat exchanger with tessellation cross-section, the temperature at the middle point of the heat exchanger was simulated. The relation diagram of temperature and mesh size in the heat exchanger is obtained as shown in **figure 21**. Therefore, 0.05 m was used as the mesh size of the heat exchanger.

DISCUSSING FINDINGS

When the heat exchanger is stable, the temperature distribution was obtained. According to **figure 22**,

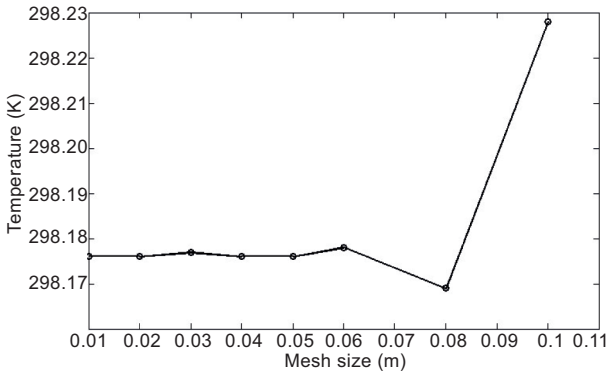

Fig. 21. Relationship between temperatures and mesh sizes.

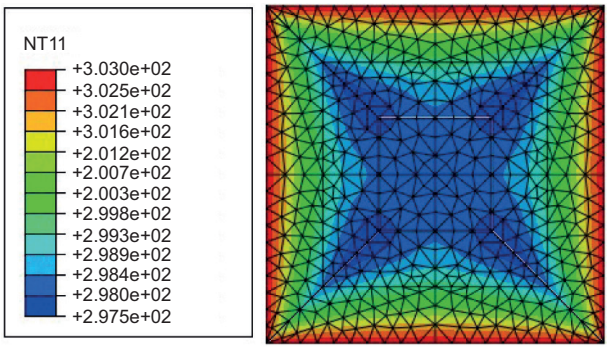

Fig. 22. Temperature distributions for the tessellation.

the maximum temperature is 303 K loaded at the boundary, the lowest temperature on the first heat exchanger is 297.5 K. Observing these two numbers, the temperature in the corresponding areas is almost the same between fractal and tessellation.

In 2019, Xu studied the phase change heat transfer process of PCM in snowflake fractal heat exchanger (Xu 2019). It takes 24950s for the heat exchanger to reach the steady state. PCM heats up from 298K to 320K, changing by 22K, and absorbs a large amount of heat. Possible explanations for the larger temperature change compared to this study are that the heat source is hotter and the heat exchanger takes longer to heat. Although his research direction is different from that of this essay, the high efficiency and accuracy of tessellation heat transfer method can still be proved by comparing the data.

CONCLUSIONS

This essay has proposed a method of fractal representation by continuous tessellation, which is used by finite element numerical analysis. In this method, the hole-fill maps were established, and the heat transfer analysis of continuous tessellation was carried out. This method was tested by comparing the results of the tessellation and corresponding pre-fractal. It is notable that the results for the first pre-fractal of fractal Vicsek and corresponding tessellation are approximately the same.

A limitation of this study is that only the tessellation of the first pre-fractal of fractal Vicsek has been tested, and it cannot prove that this method is sufficient for other situations. Therefore, the second and third pre-fractal tessellation of fractal Vicsek should be analyzed and compared with the corresponding results for pre-fractal. Notwithstanding the relatively limited sample, this work offers valuable insights into heat transfer analysis on the complex fractal heat exchangers. It is reasonable to apply this method to other fractals to verify the feasibility of this method.

FUNDING

This study was partially supported by 2020 Educational Reform Project of Zijin College, Nanjing University of Science and Technology; Key Course Group Construction of Intelligent Manufacturing for Application-oriented Undergraduates (Grant No. 20200101002).

ACKNOWLEDGMENTS

Ma Zhuqiao gratefully acknowledges the support provided by School of Intelligent Manufacturing, Nanjing University of Science and Technology, Zijin College to carry out this research work.

DATA AVAILABILITY

All data included in the present study are available on request to the author for correspondence.

REFERENCES

Begag A., Saim R., Abboudi S. and Öztop H.F. (2021). Effect of internal and external corrugated surfaces on the characteristics of heat transfer and pressure drop in a concentric tube heat exchanger. International Journal of Thermal Sciences 165. https://doi.org/10.1016/j.ijthermalsci.2021.106930

Chowdhury D., Pal M. and Ghatak R. (2018). Vicsek fractal slot substrate integrated waveguide leaky wave antenna for X-band application. Journal of Electromagnetic Waves and Applications 32 (12), 1-9. https://doi.org/10.1080/09205071.2018.1426502

Davey K., Jiang C. and Prosser R. (2016). Tessellated continuum mechanics: A Galerkin finite element method. Computers and Structures 175 (15), 157-183. https://doi.org/10.1016/j.compstruc.2016.07.003

Davey K. and Prosser R. (2013). Analytical solutions for heat transfer on fractal and pre-fractal domains. Applied Mathematical Modelling 37 (1-2), 554-569. https://doi.org/10.1016/j.apm.2012.02.047

Davey K., Prosser R. and Jiang C. (2015). Heat transfer through fractal-like porous media: A tessellated continuum approach. Computers and Structures 151, 58-72. https://doi.org/10.1016/j.compstruc.2015.01.006

Deng J., Ye Q.Q. and Wang Q. (2019). Weighted average geodesic distance of Vicsek network. Physica A: Statistical Mechanics and its Applications 527, 121327. https://doi.org/10.1016/j.physa.2019.121327

Dórea F.T. and Lemos M. (2010). Simulation of laminar impinging jet on a porous medium with a thermal non-equilibrium model. International Journal of Heat and Mass Transfer 53(23-24), 5089-5101. https://doi.org/10.1016/j.ijheatmasstransfer.2010.07.055

Feng Z.F., Hu Z.J., Lan Y.Q., Huang Z.Q. and Zhang J.X. (2021). Effects of geometric parameters of circular pin-fins on fluid flow and heat transfer in an interrupted microchannel heat sink. International Journal of Thermal Sciences 165 (1-2). https://doi.org/10.1016/j.ijthermalsci.2021.106956

Gil P. (2021). Experimental investigation on heat transfer enhancement of air-cooled heat sink using multiple synthetic jets. International Journal of Thermal Sciences 166(1). https://doi.org/10.1016/j.ijthermalsci.2021.106949

Higashiyama S., Ushijima K., Motosuke M. and Cantwell W.J. (2019). Evaluation of heat dissipation and structural response of a cellular panel as a heat exchanger. Journal of Sandwich Structures and Materials 21 (7), 2289-2312. https://doi.org/10.1177/1099636217749274

Hoq S., Okhunov A. and Tso C.P. (2020). Error estimation of bilinear Galerkin finite element method for 2D thermal problems. 3C Tecnología 9(1), 79-93. https://doi.org/10.17993/3ctecno/2020.v9n1e33.79-93

Jing F., Wang Y., Su W., Xuan B. and Li C. (2018). Heat Transfer Investigation and Modeling of Heat Integrated Distillation Column. China Petroleum Processing and Petrochemical Technology 20 (3), 96-105. https://kns.cnki.net/kcms/detail/detail.aspx? (In Chinese)

Karabanova A. Berdiyeva P., Pal M.v.d., Johnsen R.E.,Deledda S. and Blanchard D. (2021). Intrinsic kinetics in local modelling of thermochemical heat storage systems. Applied Thermal Engineering 192. https://doi.org/10.1016/j.applthermaleng.2021.116880

Kercher A.D., Corrigan A. and Kessler D.A. (2021). The moving discontinuous Galerkin finite element method with interface condition enforcement for compressible viscous flows. International Journal for Numerical Methods in Fluids 93 (5), 1490-1519. https://doi.org/10.1002/FLD.4939

Kirsanov Yu. A., Makarushkin D.V., Kirsanov A.Y. and Yudakhin A.E. (2021). Heat transfer of a stack of low-thermal-conductivity plates in cyclic heat exchange with cold and hot media. Journal of Engineering Physics and Thermophysics 94 (4), 1-12. https://doi.org/10.1007/S10891-021-02301-0

Kounadis G., Antonopoulos D.C. and Dougalis V.A. (2021). Galerkin finite element methods for the numerical solution of two classical-Boussinesq type systems over variable bottom topography. Wave Motion 102 (3). https://doi.org/10.1016/J.WAVEMOTI.2021.102715

Kounadis G., Antonopoulos D.C. and Dougalis V.A. (2021). Galerkin finite element methods for the numerical solution of two classical-Boussinesq type systems over variable bottom topography. Wave Motion 102. https://doi.org/10.1016/j.wavemoti.2021.102715

Li L.L., She M.F. and Niu Y.L. (2021). Fractional Crank-Nicolson-Galerkin finite element methods for nonlinear time fractional parabolic problems with time delay. Journal of Function Spaces (2), 1-2. https://doi.org/10.1155/2021/9981211

Li W.Z. and Hrnjak P. (2021). Compensating for the end-plate effect on heat transfer in brazed plate heat exchangers. International Journal of Refrigeration 126 (2), 99-108. https://doi.org/10.1016/j.ijrefrig.2021.01.019

Ma F., Wang X.M., Wang P. and Luo X.D. (2021). Random walks on the generalized Vicsek fractal. Europhysics Letters 133 (4), 40004. https://doi.org/10.1209/0295-5075/133/40004

Mukherjee S., Panda S.R., Mishra P.C. and Chaudhuri P. (2021). Convective flow boiling heat transfer enhancement with aqueous Al_2O_3 and TiO_2 nanofluids: Experimental investigation. International Journal of Thermophysics 42 (6). https://doi.org/10.1007/S10765-021-02850-9

Nwosu N.P. (2009). Finite-element analysis of an absorber in an evacuated solar tube heat exchanger employing the Galerkin method. International Journal of Sustainable Energy 28 (4), 247-255. https://doi.org/10.1080/14786450903295853

Pimenta F. and Alves M.A. (2021). Conjugate heat transfer in the unbounded flow of a viscoelastic fluid past a sphere.

International Journal of Heat and Fluid Flow 89(3). https://doi.org/10.1016/j.ijheatfluidflow.2021.108784

Teamah M.A., EI-Maghlany W.M. and Dawood M.M.K. (2011). Numerical simulation of laminar forced convection in horizontal pipe partially or completely filled with porous material. International Journal of Thermal Sciences 50 (8), 1512-1522. https://doi.org/10.1016/j.ijthermalsci.2011.03.003

Thinh, Kie. (2017). Galerkin finite element method for generalized Forchheimer equation of slightly compressible fluids in porous media. Mathematical Methods in the Applied Sciences 40 (12), 4364-4384. https://doi.org/10.1002/mma.4310

Tian J., Lu T.J., Hodson H.P., Queheillalt D.T. and Wadley H.N.G. (2007). Cross flow heat exchange of textile cellular metal core sandwich panels. International Journal of Heat and Mass Transfer 50 (13-14), 2521-2536. https://doi.org/10.1016/j.ijheatmasstransfer.2006.11.042

Xu H. (2019). Study on Heat Transfer Characteristics of PCM Melting in a Fractal Heat Exchanger. Master's thesis. Suzhou University of Science and Technology. Suzhou, China, 84 pp.

Ye X. and Zhang S.Y. (2020). A stabilizer-free weak Galerkin finite element method on polytopal meshes. Journal of Computational and Applied Mathematics 371(C), 112699. https://doi.org/10.1016/j.cam.2019.112699

Yuan B., Yang W., Zhang S., Zhang B. and Ying Y. (2020). Numerical simulation of multi-physics processes in nuclear system based on Galerkin finite element method. 2020 International Conference on Nuclear Engineering collocated with the ASME 2020 Power Conference. https://doi.org/10.1115/ICONE2020-16801

Zhang T. and Zhang S.Y. (2020). The weak Galerkin finite element method for the transport-reaction equation. Journal of Computational Physics 410 (C), 109399. https://doi.org/10.1016/j.jcp.2020.109399

APPENDIX

The corresponding cover maps for the Vicsek fractal

$$P_1(x,y)=\begin{cases}P_{11}(x,y) & for\ area1\ in\ Figure\ 3\\ P_{12}(x,y) & for\ area2\ in\ Figure\ 3\\ P_{13}(x,y) & for\ area3\ in\ Figure\ 3\\ P_{14}(x,y) & for\ area4\ in\ Figure\ 3\\ P_{15}(x,y) & for\ area5\ in\ Figure\ 3\\ P_{16}(x,y) & for\ area6\ in\ Figure\ 3\\ P_{17}(x,y) & for\ area7\ in\ Figure\ 3\\ P_{18}(x,y) & for\ area8\ in\ Figure\ 3\end{cases}\quad P_2(x,y)=\begin{cases}P_{21}(x,y) & for\ area1\ in\ Figure\ 3\\ P_{22}(x,y) & for\ area2\ in\ Figure\ 3\\ P_{23}(x,y) & for\ area3\ in\ Figure\ 3\\ P_{24}(x,y) & for\ area4\ in\ Figure\ 3\\ P_{25}(x,y) & for\ area5\ in\ Figure\ 3\\ P_{26}(x,y) & for\ area6\ in\ Figure\ 3\\ P_{27}(x,y) & for\ area7\ in\ Figure\ 3\\ P_{28}(x,y) & for\ area8\ in\ Figure\ 3\end{cases}$$

$$P_3(x,y)=\begin{cases}P_{31}(x,y) & for\ area1\ in\ Figure\ 3\\ P_{32}(x,y) & for\ area2\ in\ Figure\ 3\\ P_{33}(x,y) & for\ area3\ in\ Figure\ 3\\ P_{34}(x,y) & for\ area4\ in\ Figure\ 3\\ P_{35}(x,y) & for\ area5\ in\ Figure\ 3\\ P_{36}(x,y) & for\ area6\ in\ Figure\ 3\\ P_{37}(x,y) & for\ area7\ in\ Figure\ 3\\ P_{38}(x,y) & for\ area8\ in\ Figure\ 3\end{cases}\quad P_4(x,y)=\begin{cases}P_{41}(x,y) & for\ area1\ in\ Figure\ 3\\ P_{42}(x,y) & for\ area2\ in\ Figure\ 3\\ P_{43}(x,y) & for\ area3\ in\ Figure\ 3\\ P_{44}(x,y) & for\ area4\ in\ Figure\ 3\\ P_{45}(x,y) & for\ area5\ in\ Figure\ 3\\ P_{46}(x,y) & for\ area6\ in\ Figure\ 3\\ P_{47}(x,y) & for\ area7\ in\ Figure\ 3\\ P_{48}(x,y) & for\ area8\ in\ Figure\ 3\end{cases}$$

$$P_5(x,y)=\begin{cases}P_{51}(x,y) & for\ area1\ in\ Figure\ 3\\ P_{52}(x,y) & for\ area2\ in\ Figure\ 3\\ P_{53}(x,y) & for\ area3\ in\ Figure\ 3\\ P_{54}(x,y) & for\ area4\ in\ Figure\ 3\\ P_{55}(x,y) & for\ area5\ in\ Figure\ 3\\ P_{56}(x,y) & for\ area6\ in\ Figure\ 3\\ P_{57}(x,y) & for\ area7\ in\ Figure\ 3\\ P_{58}(x,y) & for\ area8\ in\ Figure\ 3\end{cases}$$

Where

$$P_{11}(x,y)=\left(\frac{x}{3},-\frac{x}{3}+\frac{2y}{3}+\frac{1}{3}\right),P_{12}(x,y)=\left(\frac{x}{3},\frac{y}{3}+\frac{1}{3}\right),P_{13}(x,y)=\left(\frac{x}{3},\frac{y}{3}+\frac{1}{3}\right),P_{14}(x,y)=\left(\frac{x}{3},\frac{x}{3}+\frac{2y}{3}\right),$$

$$P_{15}(x,y)=\left(\frac{x}{3},\frac{x}{3}+\frac{2y}{3}\right),P_{16}(x,y)=\left(\frac{x}{3},y\right),P_{17}(x,y)=\left(\frac{x}{3},y\right),P_{18}(x,y)=\left(\frac{x}{3},-\frac{x}{3}+\frac{2y}{3}+\frac{1}{3}\right);$$

$$P_{21}(x,y)=\left(\frac{x}{3}+\frac{1}{3},\frac{y}{3}+\frac{1}{3}\right),P_{22}(x,y)=\left(\frac{x}{3}+\frac{1}{3},\frac{y}{3}+\frac{1}{3}\right)\ P_{23}(x,y)=\left(\frac{x}{3}+\frac{1}{3},\frac{y}{3}+\frac{1}{3}\right),P_{24}(x,y)=\left(\frac{x}{3}+\frac{1}{3},\frac{y}{3}+\frac{1}{3}\right),$$

$$P_{25}(x,y)=\left(\frac{x}{3}+\frac{1}{3},\frac{y}{3}+\frac{1}{3}\right),P_{26}(x,y)=\left(\frac{x}{3}+\frac{1}{3},\frac{y}{3}+\frac{1}{3}\right)\ P_{27}(x,y)=\left(\frac{x}{3}+\frac{1}{3},\frac{y}{3}+\frac{1}{3}\right),P_{28}(x,y)=\left(\frac{x}{3}+\frac{1}{3},\frac{y}{3}+\frac{1}{3}\right);$$

$$P_{31}(x,y)=\left(\frac{x}{3}+\frac{1}{3},\frac{y}{3}\right),P_{32}(x,y)=\left(\frac{2x}{3}-\frac{y}{3}+\frac{1}{3},\frac{y}{3}\right),P_{33}(x,y)=\left(\frac{2x}{3}-\frac{y}{3}+\frac{1}{3},\frac{y}{3}\right),P_{34}(x,y)=\left(x,\frac{y}{3}\right),$$

$$P_{35}(x,y)=\left(x,\frac{y}{3}\right),P_{36}(x,y)=\left(\frac{2x}{3}+\frac{y}{3},\frac{y}{3}\right),P_{37}(x,y)=\left(\frac{2x}{3}+\frac{y}{3},\frac{y}{3}\right),P_{38}(x,y)=\left(\frac{x}{3}+\frac{2}{3},\frac{y}{3}\right);$$

$$P_{41}(x,y)=\left(\frac{x}{3}+\frac{2}{3},\frac{x}{3}+\frac{2y}{3}\right),P_{42}(x,y)=\left(\frac{x}{3}+\frac{2}{3},y\right),P_{43}(x,y)=\left(\frac{x}{3}+\frac{2}{3},y\right),P_{44}(x,y)=\left(\frac{x}{3}+\frac{2}{3},-\frac{x}{3}+\frac{2y}{3}+\frac{1}{3}\right),$$

$$P_{45}(x,y)=\left(\frac{x}{3}+\frac{2}{3},-\frac{x}{3}+\frac{2y}{3}+\frac{1}{3}\right),P_{46}(x,y)=\left(\frac{x}{3}+\frac{2}{3},\frac{y}{3}+\frac{1}{3}\right),P_{47}(x,y)=\left(\frac{x}{3}+\frac{2}{3},\frac{y}{3}+\frac{1}{3}\right),P_{48}(x,y)=\left(\frac{x}{3}+\frac{2}{3},\frac{x}{3}+\frac{2y}{3}\right);$$

$$P_{51}(x,y)=\left(x,\frac{y}{3}+\frac{2}{3}\right),P_{52}(x,y)=\left(\frac{2x}{3}+\frac{y}{3},\frac{y}{3}+\frac{2}{3}\right),P_{53}(x,y)=\left(\frac{2x}{3}+\frac{y}{3},\frac{y}{3}+\frac{2}{3}\right),P_{54}(x,y)=\left(\frac{x}{3}+\frac{1}{3},\frac{y}{3}+\frac{2}{3}\right),$$